nature plants

Article

https://doi.org/10.1038/s41477-022-01261-4

A legume kinesin controls vacuole morphogenesis for rhizobia endosymbiosis

Received: 8 November 2018

Accepted: 9 September 2022

Published online: 31 October 2022

Check for updates

Xiaxia Zhang[1], Qi Wang[1], Jingxia Wu[1], Meifang Qi[2], Chen Zhang[1], Yige Huang[1], Guangda Wang[1], Huan Wang[1], Juan Tian[1], Yanjun Yu[1], Dasong Chen[3], Youguo Li[3], Dong Wang[4], Yijing Zhang[2], Yongbiao Xue[5] and Zhaosheng Kong[1,6]

Symbioses between legumes and rhizobia require establishment of the plant-derived symbiosome membrane, which surrounds the rhizobia and accommodates the symbionts by providing an interface for nutrient and signal exchange. The host cytoskeleton and endomembrane trafficking systems play central roles in the formation of a functional symbiotic interface for rhizobia endosymbiosis; however, the underlying mechanisms remain largely unknown. Here we demonstrate that the nodulation-specific kinesin-like calmodulin-binding protein (nKCBP), a plant-specific microtubule-based kinesin motor, controls central vacuole morphogenesis in symbiotic cells in *Medicago truncatula*. Phylogenetic analysis further indicated that *nKCBP* duplication occurs solely in legumes of the clade that form symbiosomes. Knockout of *nKCBP* results in central vacuole deficiency, defective symbiosomes and abolished nitrogen fixation. nKCBP decorates linear particles along microtubules, and crosslinks microtubules with the actin cytoskeleton, to control central vacuole formation by modulating vacuolar vesicle fusion in symbiotic cells. Together, our findings reveal that rhizobia co-opted *nKCBP* to achieve symbiotic interface formation by regulating cytoskeletal assembly and central vacuole morphogenesis during nodule development.

Legume–rhizobia symbiosis enables the development of root nodules that fix nitrogen for plant use and for the terrestrial nitrogen cycle[1,2]. Mutualistic interactions between rhizobia and host legumes have co-opted a variety of host developmental programmes and generated specialized symbiotic tissues and organs[3,4]. In most legume species, the rhizobia are entrapped in the host through curling root hairs, and then proliferate in the tubular infection threads (ITs) enveloped by the host-derived membrane[5,6]. Simultaneously, nodule organogenesis occurs in dividing pericycle and cortical cells under the infection foci[3,5]. The IT elongates towards the developing nodule primordium, and the bacteria are released from the ITs into the cytoplasm of nodule cells in the form of infection droplets[7–9]. The released rhizobia differentiate into long rod-like bacteroids, which remain encased within the plant-derived membrane system, finally forming the basic nitrogen-fixing unit, the symbiosome[10]. The symbiosome membrane system in infected nodule cells undergoes massive proliferation and dynamic organization to accommodate symbiotic rhizobia that efficiently fix nitrogen[10–12]. Components of the plant cytoskeleton (microtubules and actin filaments, F-actin) play central roles in cellular organization and intracellular transport[13,14], and form distinct architectures to support IT

[1]State Key Laboratory of Plant Genomics, Institute of Microbiology, Innovative Academy of Seed Design, Chinese Academy of Sciences, Beijing, China. [2]State Key Laboratory of Plant Molecular Genetics, Center for Excellence in Molecular Plant Science, Chinese Academy of Sciences, Shanghai, China. [3]State Key Laboratory of Agricultural Microbiology, Huazhong Agricultural University, Wuhan, China. [4]Department of Biochemistry and Molecular Biology, University of Massachusetts, Amherst, MA, USA. [5]State Key Laboratory of Plant Cell and Chromosome Engineering, Institute of Genetics and Developmental Biology, Chinese Academy of Sciences, Beijing, China. [6]Houji Laboratory in Shanxi Province, Academy of Agronomy, Shanxi Agricultural University, Taiyuan, China. e-mail: zskong@im.ac.cn

growth, infection droplet formation and bacterial release, as well as accommodation of symbiosomes during root nodule symbiosis[15–17].

The central vacuole, the largest organelle in plant cells, is required for plant cell differentiation, defining intracellular compartmentation and providing turgor force[18]. In particular, vacuolar dynamics and central vacuole morphogenesis play essential roles in forming functional symbiosomes to host symbiotic rhizobia[19]. Uptake of bacteria into living host plant cells has been considered as the holy grail in the evolution of root nodule symbiosis[20]. However, it remains largely unknown how host cells modulate intricate membrane dynamics to maintain proper turgor pressure and cell integrity during rhizobia accommodation, and how the cytoskeleton integrates with the endomembrane system to regulate the formation of a functional host–microbe interface, especially for central vacuole formation, during symbiotic cell differentiation.

Kinesin-like calmodulin-binding protein (KCBP) is a microtubule-based kinesin motor found uniquely within the plant kingdom[21–23]. It contains a fused MyTH4-FERM domain, which occurs in only some myosin (F-actin-based motor protein) families outside plants, so KCBP has been regarded as an evolutionary chimaera of kinesin and myosin[21,22]. Our previous studies revealed that KCBP acts as a hub protein integrating microtubules with F-actin to control trichome cell morphogenesis in *Arabidopsis*, and provided direct evidence that the FERM motif directly binds F-actin[24]. Intriguingly, the *Marchantia polymorpha* KCBP is required for rhizoid growth, which is thought to have been essential for the earliest plants to adapt to life on land 400 million years ago[25,26]. Recent transcriptomic studies revealed that a *Medicago truncatula* KCBP orthologue (Medtr8g072430) is ubiquitously expressed in various organs and upregulated in root hairs at the IT formation stage[27]. In this Article, we report that the *M. truncatula* genome contains another KCBP-encoding gene, which is nodule enriched and thus designated *nKCBP*. Further studies revealed that the duplication of KCBP genes occurred solely in legume–rhizobia interactions able to form advanced symbiosomes. Remarkably, rhizobia hijack the nodulation-enriched KCBP to crosslink microtubules with the actin cytoskeleton to modulate central vacuole formation in symbiotic cells, thus achieving symbiosome development and nitrogen fixation.

Results

Gene duplication in legumes produces a nodule-enriched *KCBP* copy

On the basis of the infectome data[27], we further made BLAST analysis of KCBP proteins and uncovered a duplication of KCBP-encoding genes in *M. truncatula*: one *KCBP* paralogue (Medtr8g072430) is ubiquitously expressed in various tissues, and another *KCBP* paralogue (Medtr5g025100), *nKCBP*, is predominantly expressed in nodules at various developmental stages and decreases after a 2 day nitrate treatment[28] (Supplementary Fig. 1a). We validated the expression levels by quantitative reverse-transciption polymerase chain reaction (qRT–PCR; Fig. 1a) and further confirmed the nodule-enriched expression pattern of *nKCBP* by expressing the *GUS* reporter gene (encoding β-glucuronidase) under the control of its native promoter (2,185 bp upstream of ATG) in transgenic hairy roots.

Histochemical staining showed strong expression in nodules at 7 and 14 days post-inoculation (dpi) with *Sinorhizobium meliloti* 2011 (Fig. 1b,c). Longitudinal sections of 14 dpi nodules revealed a stronger expression of *nKCBP* in zone II and the infected cells of nitrogen-fixing zone III (Fig. 1c).

To obtain evolutionary insights into the function of *nKCBP* during root nodule symbiosis, we conducted a phylogenetic analysis using 26 representative species from 14 families of flowering plants with available genome sequences (Fig. 1d). Unexpectedly, we uncovered that diploid leguminous plants have two copies of *KCBP* in their genomes (such as *M. truncatula* and *Lotus japonicus*), whereas there is only one *KCBP* in diploid dicots of another 11 families, and in two diploid monocots of the Graminaceae family, *Oryza sativa* and *Brachypodium distachyon* (Fig. 1d). Accordingly, there are two copies of *KCBP* in the allotetraploid *Gossypium hirsutum*[29] and *Linum usitatissimum*[30], as well as in the ancient tetraploid *Populus trichocarpa*[31], whereas there are four copies in *Glycine max*, another ancient tetraploid[32]. Furthermore, transcriptional data showed that the corresponding duplicated *KCBP* copies in *G. max*, *L. japonicus* and *Phaseolus vulgaris* also show predominant expression in nodules (Supplementary Fig. 1b–d). Interestingly, duplication of KCBP-encoding genes occurred solely in legumes that form symbiosomes, which represent a more advanced symbiotic form[33]. By contrast, *KCBP* duplication did not occur in *Cercis canadensis* of the Fabaceae subfamily Caesalpinoideae and the only non-legume nodulating species *Parasponia andersonii* (Fig. 1d), which forms primitive symbiotic organs, termed fixation threads, to fix nitrogen[33,34]. Taken together, these results suggested that the duplication of *KCBP* occurs solely in legumes that form mutualism with rhizobia, and most likely, this duplication event is associated with legume–rhizobia symbiosis.

nKCBP functions in nodule development and nitrogen fixation

To gain genetic insight into the function of *nKCBP*, we generated stable knockout mutants using clustered regularly interspaced short palindromic repeats (CRISPR)/Cas9-mediated technology. We obtained two alleles (Fig. 2), *nkcbp-1* and *nkcbp-2*, which were validated as null alleles caused by premature stop codons at amino acids 72 and 44, respectively (Supplementary Fig. 2a). Both *nkcbp* mutants exhibited symptoms of nitrogen starvation under symbiotic (nitrogen-free) growth conditions (Fig. 2a) compared with the wild-type (WT) control; the mutants had no distinct phenotype for leaf trichomes or root hairs (Supplementary Fig. 2b–i). Strikingly, the growth retardation caused by nitrogen starvation in *nkcbp* mutants was rescued when they were supplied with ammonium nitrate, indicating that loss of *nKCBP* function resulted in nitrogen starvation associated with defective nitrogen fixation (Supplementary Fig. 3a). Indeed, the nodules of *nkcbp* mutants were light pink at 28 dpi with *S. meliloti* 2011, whereas fully elongated WT nodules were red (Fig. 2b). We further analysed nodule number and nodule size, and found that the nodule number of the mutants showed no difference compared with WT (Fig. 2c), while the nodule size of *nkcbp* mutants markedly decreased (Fig. 2d). Acetylene reduction assays demonstrated that nitrogenase activity in *nkcbp* nodules was dramatically lower than in WT (Fig. 2e). These results indicate that nKCBP is required for proper nodule development and robust nitrogen fixation.

nkcbp mutants exhibit defects in central vacuole formation

To elucidate the mechanisms by which *nKCBP* regulates nodule development and nitrogen fixation, we examined the morphology of cells in nodules during development. *M. truncatula* forms the indeterminate nodules, which possess typical zones: a persistent meristem (zone I), infection zone (zone II), interzone (IZ) and nitrogen-fixing zone (zone III) from the nodule tip to base[9]. We first selected two representative nodule developmental stages, 10 dpi and 21 dpi. Although *nkcbp* nodules show characteristic zonation as observed in the WT control, infected cells (symbiotic cells) lose the central vacuole (Fig. 3a–f). In particular, infected cells of nitrogen-fixing zones in WT nodules have prominent and large central vacuoles (Fig. 3b,c), while infected cells in *nkcbp* mutants exhibit numerous randomly distributed small, unfused vacuoles (Fig. 3e,f). The vacuole formation defects specifically occur in infected cells of *nkcbp* nodules, whereas uninfected cells have a large central vacuole (Fig. 3c,f). Notably, external nitrogen application did not rescue intrinsic vacuole developmental defects in infected cells but indeed restored the dwarf growth phenotype (Supplementary Fig. 3a–e), further confirming that nitrogen starvation symptoms of *nkcbp* mutants are caused by vacuole developmental defects in infected cells. To demonstrate vacuole morphogenesis in live nodule cells, we used the VAMP711 (refs. [35,36]) (the tonoplast-localized SNARE protein) to label the tonoplast in nodules by hairy-root transformation. In the *nkcbp* mutant, numerous small vacuoles were observed to be randomly

https://doi.org/10.1038/s41477-022-01261-4

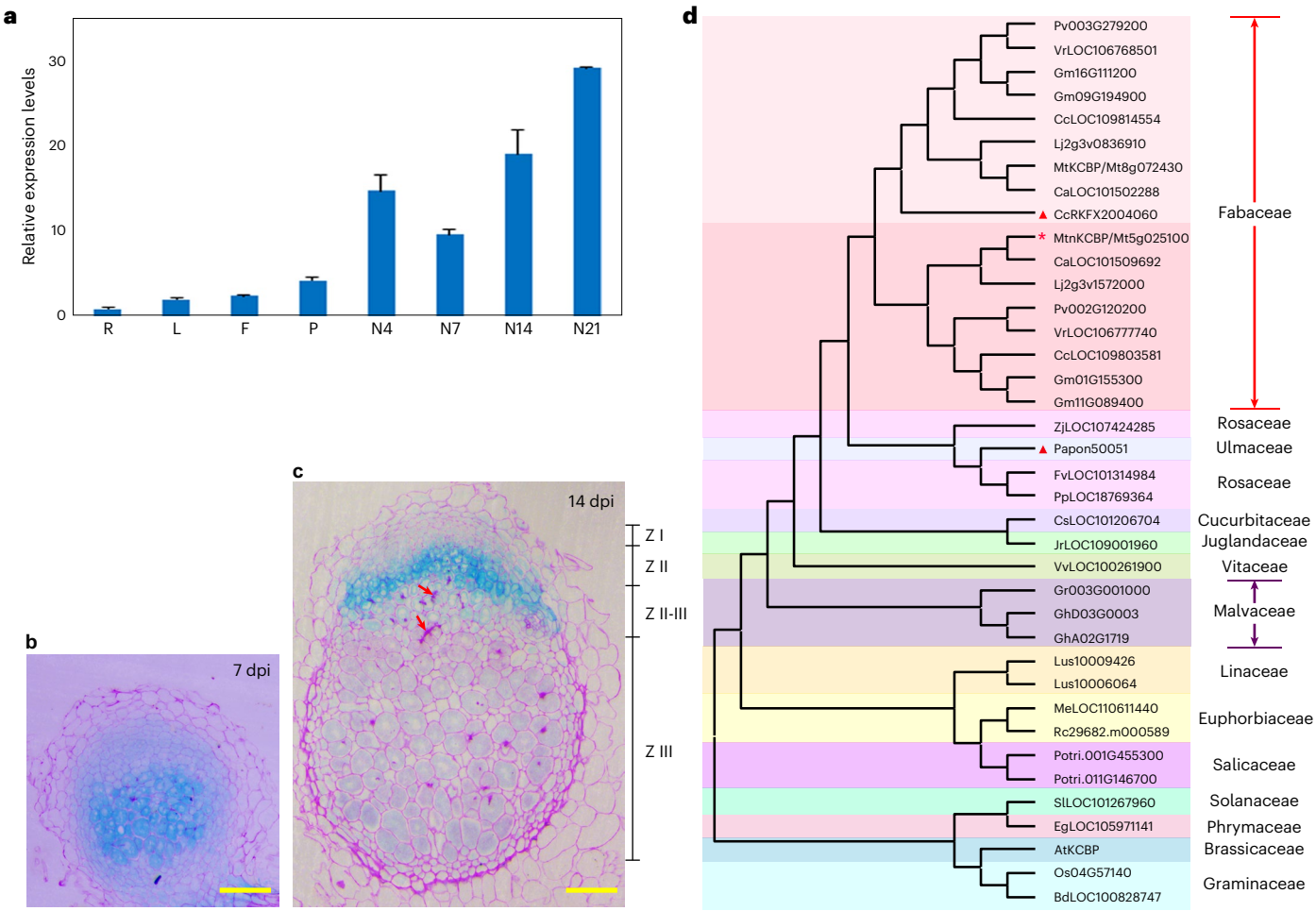

Fig. 1 | Expression patterns of *M. truncatula nKCBP*, and phylogenetic analysis of KCBP proteins in flowering plants. a, Analysis of *nKCBP* expression in different tissues by qRT–PCR. Total RNAs from roots, leaves, young flowers, pods and nodules at 4, 7, 14 and 21 dpi were used for assays. *MtACTIN11* was used as the reference gene. A representative example out of three biological experiments is shown, and error bars represent mean ± standard deviation (s.d.) for three technical replicates. **b**,**c**, Nodules at 7 dpi (**b**) and 14 dpi (**c**) were dissected from *Medicago* transgenic hairy roots expressing the β-glucuronidase (*GUS*) reporter under the control of the *nKCBP* promoter, and were stained with GUS solution for semi-section. Then, ruthenium red staining was performed for imaging. The transformation-positive hairy roots for GUS staining were from at least 54 plants with three biological replicates. A representative image out of three biological experiments is shown. Meristem (zone I, ZI), infection zone (zone II, ZII), interzone (IZ, ZII–III) and nitrogen-fixing zone (zone III, ZIII). Red arrows mark the infected threads. **d**, Phylogenetic tree of KCBPs of 26 species in 14 families of flowering plants, including Fabaceae, Cucurbitaceae, Juglandaceae, Rosaceae, Umlaceae, Solanaceae, Phrymaceae, Vitaceae, Malvaceae, Euphorbiaceae, Salicaceae, Linaceae, Brassicaceae and Graminaceae. The red asterisk indicates a duplicated *KCBP* paralogue, *MtnKCBP*. Red triangles indicate *KCBP* orthologues in *Cercis canadensis* and *Parasponia andersonii*. Scale bars, 100 μm (**b** and **c**).

distributed among symbiosomes of infected cells of nitrogen-fixing zones, while the central vacuole was seen in WT (Fig. 3g,h and Supplementary Movie 1). To further illustrate vacuole morphogenesis at nanometre resolution, we performed AutoCUTS-SEM (automatic collector of ultrathin sections scanning electron microscopy)[37] to obtain the high-resolution reconstruction of symbiotic cells in three dimensions. We found that vacuoles in zone I and zone II are unfused, showing small vesicles in both WT and the *nkcbp* mutant. However, in zone III, only infected cells of the *nkcbp* mutant do not form the big central vacuoles, while uninfected cells (100%) of the *nkcbp* mutant and all the nodule cells of the WT form the central vacuoles (Supplementary Fig. 4). Furthermore, we reconstructed the intact central vacuole in symbiotic cells of WT (Fig. 3i and Supplementary Movies 2 and 4), but reconstructed only small vacuoles of various sizes, which were scattered among symbiosomes in symbiotic cells of the *nkcbp* mutant (Fig. 3j and Supplementary Movies 3 and 5). Taken together, these results clearly indicate that nKCBP is required for vacuole fusion and central vacuole formation in symbiotic cells during root nodule symbiosis.

nKCBP regulates symbiosome development and bacteroid differentiation

To further gain insight into the role of nKCBP in symbiosome development, we carefully examined scanning electron microscopy (SEM) images of high resolution. The rhizobia in ITs displayed no difference between the *nkcbp* mutant and the WT (Fig. 4a,b). However, at the nitrogen-fixing zone, symbiotic cells of *nkcbp* mutants contain a considerable portion of bacteroids showing incomplete differentiation or impaired development, even with an abnormally enlarged peribacteroid space (Fig. 4d,f), while in WT there were well-developed symbiosomes (Fig. 4c,e). Intriguingly, benefitting from the high-resolution AutoCUTS-SEM, we observed that there were many undifferentiated bacteroids (different from the normal rhizobia and symbiosomes) in central vacuoles of WT symbiotic cells (Fig. 4c). However, undifferentiated bacteroids were seldom seen in vacuoles of the *nkcbp* mutant; they instead largely accumulated in the cytoplasm (Fig. 4d). Taken together, these observations indicate that loss of *nKCBP* function results in the failure of vacuolar fusion and symbiosome membrane formation, and

https://doi.org/10.1038/s41477-022-01261-4

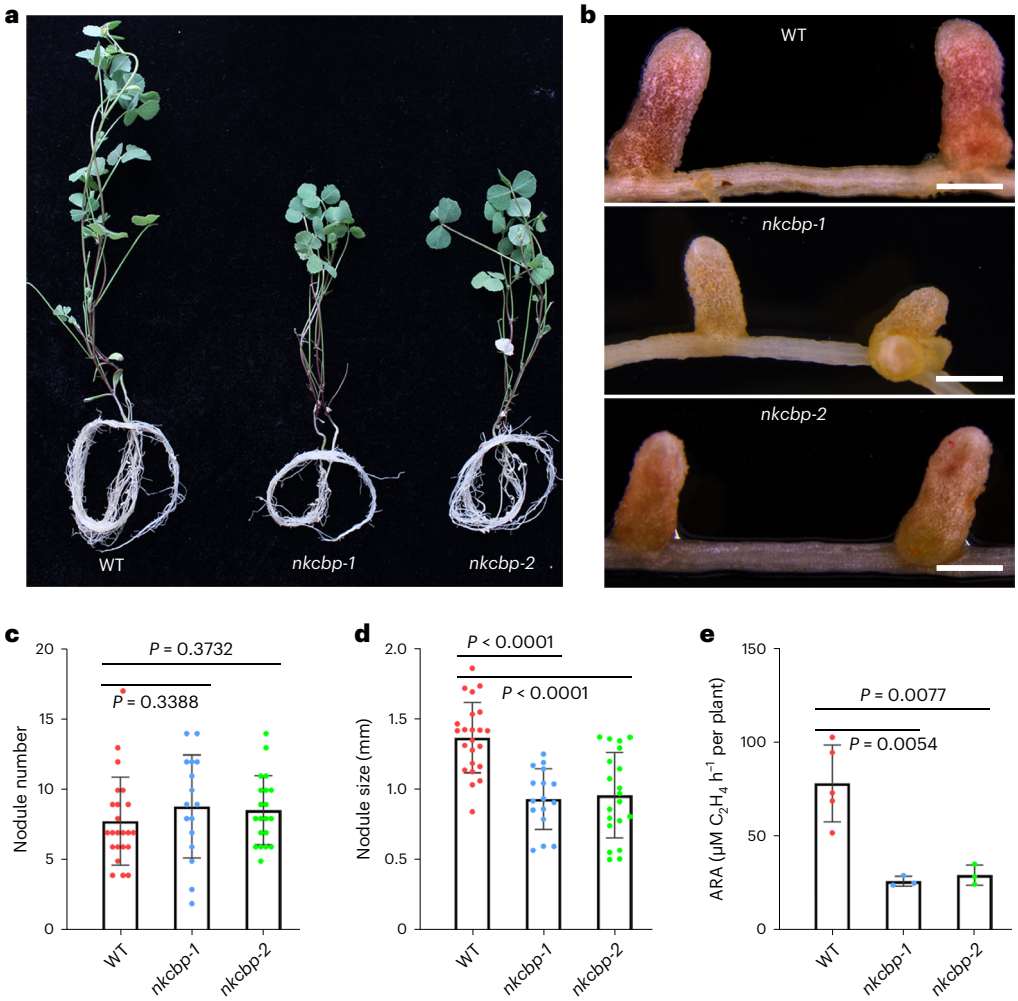

Fig. 2 | *M. truncatula nkcbp* mutants exhibited nitrogen starvation symptoms and nodule developmental defects. a, *nkcbp* mutants show nitrogen starvation symptoms at 28 dpi under symbiotic growth conditions (nitrogen free, but with *S. meliloti* 2011 strain applied). WT R108 plants were used as the control. **b**, *nkcbp* nodules at 28 dpi are smaller and light pink, in contrast to fully elongated, red nodules in WT. The experiments were performed with three independent replicates; $n = 36$. **c**,**d**, Nodule number and nodule size of WT and *nkcbp* mutants. The nodules were collected at 21 dpi with three biological replicates. The dots represent the value of number (**c**) and size (**d**) per plant. Dots indicate the values of three biological replicates. Error bars indicate mean ± s.d. Statistical significance of the differences was tested using the multiple two-sided Student's *t*-test (WT, $n = 23$; *nkcbp-1*, $n = 16$; *nkcbp-2*, $n = 20$). Significant differences: (in **c**, WT versus *nkcbp-1*: $P = 0.3388$; WT versus *nkcbp-2*: $P = 0.3732$), (in **d**, WT versus *nkcbp-1*: $P < 0.0001$; WT versus *nkcbp-2*: $P < 0.0001$). **e**, Acetylene reduction assay (ARA) revealed significantly decreased nitrogen-fixing activities of both *nkcbp-1* and *nkcbp-2* nodules at 28 dpi. Each dot represents the mean value of six plants (WT, $n = 5$; *nkcbp-1*, $n = 3$; *nkcbp-2*, $n = 3$). Error bars indicate mean ± s.d. Statistical significance of the differences was tested using the multiple two-sided Student's *t*-test. Significant differences: WT versus *nkcbp-1*: $P = 0.0054$; WT versus *nkcbp-2*: $P = 0.0077$. Scale bars, 1 mm (**b**).

consequently impairs symbiosome development and recycling of undifferentiated bacteroids during rhizobia accommodation and nitrogen fixation. In view of the known correlation between rhizobium size and ploidy, we measured the ploidy of bacteroid of the *nkcbp* mutant and WT nodules. The flow cytometry assay demonstrated that the ploidy distribution of bacteroids in the *nkcbp* mutant showed a clear shift to lower levels compared with that of the WT (Fig. 4g), further confirming the observations of defective symbiosomes in infected cells of the *nkcbp* mutant (Fig. 4d,f).

Dual binding capability of nKCBP to microtubules and actin filaments

To investigate the mechanistic contribution of nKCBP to vacuolar construction during symbiosome development, we examined the subcellular localization of nKCBP. We generated stable transgenic *M. truncatula* plants expressing *nKCBP-GFP* driven by the native *nKCBP* promoter, which could fully complement the vacuole defect in the *nkcbp* mutant (Supplementary Fig. 5a,b). In zone III, live-cell imaging revealed that nKCBP-GFP fluorescence signals were specifically observed in infected cells but not in uninfected cells (122 cells in 20 nodules were tested, including 70 infected cells and 52 uninfected cells). In symbiotic cells, nKCBP decorates linear vesicle-like particles, with some closely associated with symbiosome membranes, and others in peri-symbiont space (Fig. 5a and Supplementary Movie 6). Furthermore, we observed the co-localization of nKCBP-GFP with microtubules (immunofluorescence labelling) and F-actin (stained with tetramethylrhodamine isothiocyanate (TRITC)–phalloidin) in symbiotic cells. The results showed that, in infected cells, MtnKCBP localizes in a linear punctate pattern with microtubules (Fig. 5b), with a few nKCBP particles binding to actin filaments (Fig. 5c). Previously, we revealed that microtubule-based KCBP kinesin binds to F-actin via the FERM domain in *Arabidopsis*[24]. Therefore, we visualized the localization pattern of nKCBP using the transient overexpression system of *Agrobacterium*-infiltrated *Nicotiana benthamiana* leaves, and validated that the full-length nKCBP decorates

https://doi.org/10.1038/s41477-022-01261-4

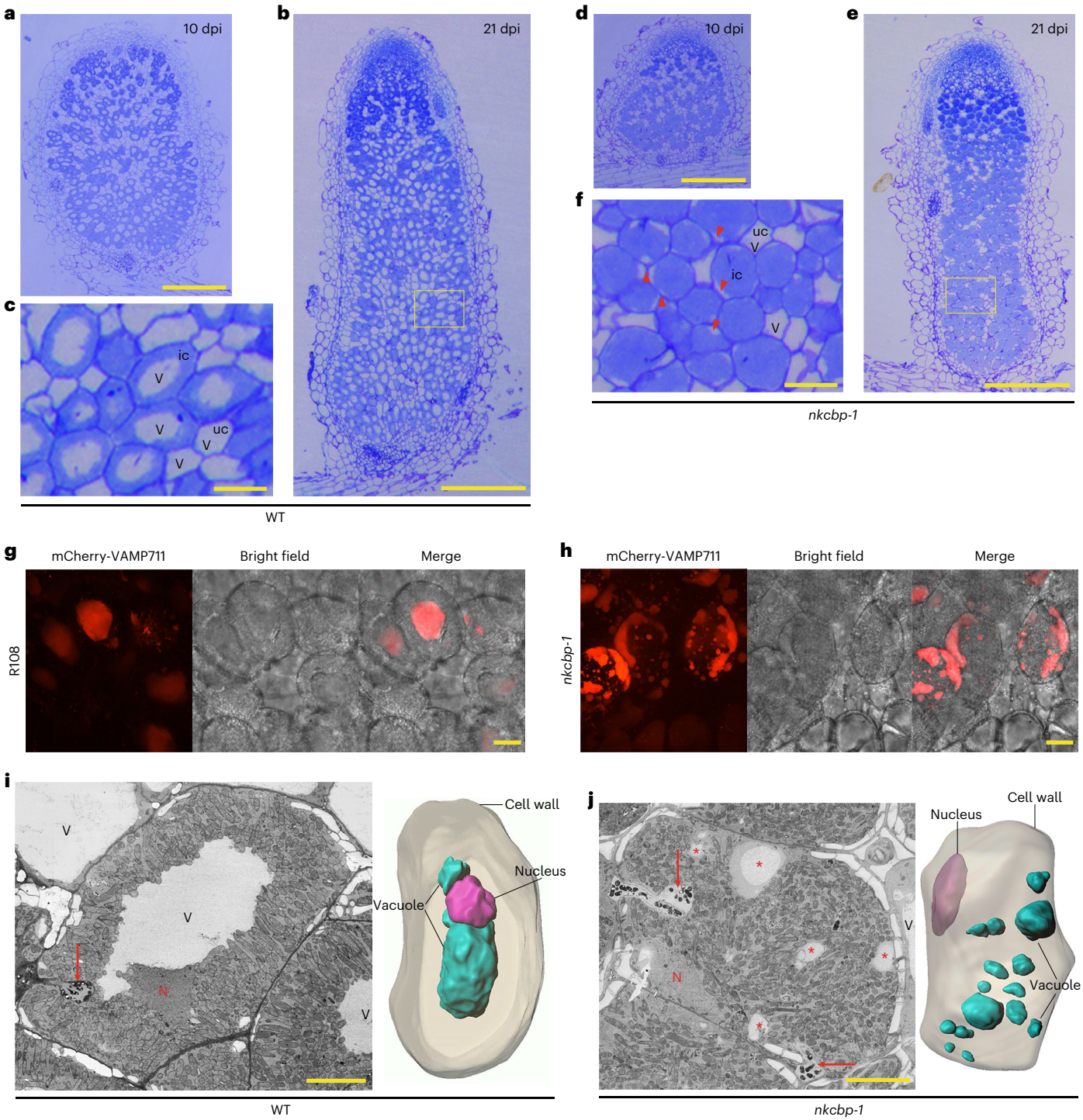

Fig. 3 | Loss of *nKCBP* function disrupts the formation of the central vacuole in symbiotic cells. a–**f**, Semi-thin sections of nodules stained with 0.4% toluidine blue. In **a**–**c**, infected WT cells at the nitrogen-fixing zone possess a single large central vacuole at 10 dpi (**a**) and 21 dpi (**b**). Close-up view of the boxed area in **b** is shown in **c**. In **d**–**f**, infected *nkcbp* cells at the nitrogen-fixing zone lose the central vacuole at 10 dpi (**d**) and 21 dpi (**e**). Close-up view of the boxed area in **e** is shown in **f**. Infected cells have numerous fragmented vacuoles at the cell margin, indicated by red arrowheads, whereas uninfected cells still have a large central vacuole. **g**–**j**, In WT nodules, both infected cells and uninfected cells have a large central vacuole (**g**, confocal image; **i**, AutoCUTS-SEM reconstruction). By contrast, in *nkcbp* nodules, central vacuole formation is completely abolished in infected cells, with several small vacuoles at the cell periphery, whereas the central vacuole still exists in uninfected cells (**h**, confocal image; **j**, AutoCUTS-SEM reconstruction). The nodules for semi-thin section were collected from at least 72 plants of three biological replicates, and nodules for confocal observation and SEM reconstruction were randomly selected from 36 plants with at least three biological replicates. The images are maximum projections of 49 *Z*-slices (**g**) and 68 *Z*-slices (**h**), 0.3 µm per step size. ic, infected cells; uc, uninfected cells; V, central vacuoles; N, nuclei; red asterisks indicate small vacuoles in infected *nkcbp* cells; red arrows mark the infected threads. Scale bars, 0.4 mm (**a**, **b**, **d** and **e**), 50 µm (**c** and **f**), 10 µm (**g** and **h**) and 20 µm (**i** and **j**).

microtubules and the FERM domain binds to F-actin, further confirming the conserved biochemical function for KCBP motor to integrate microtubules with F-actin (Supplementary Fig. 5c,d).

nKCBP modulates cytoskeletal organization to control vacuole formation

The cytoskeleton plays critical roles during vacuolar fusion and central vacuole formation[38–41]. Therefore, we next observed the cytoskeleton (microtubules and F-actin) organization in infected cells of WT and *nkcbp* nodules. In infected cells of WT nodules, endoplasmic microtubule bundles were oriented mainly parallel to symbiosomes (Fig. 5d) and associated with individual symbiosomes[15]. However, endoplasmic microtubules formed disorganized networks in the cytoplasm of infected cells in *nkcbp* nodules (Fig. 5d). The F-actin filaments align radially around the central vacuole, while disorganized short F-actin fragments were seen distributed randomly in the cytoplasm of infected cells in *nkcbp* nodules (Fig. 5e). Furthermore, we investigated symbiosome development, and compared symbiosome organization between WT and *nkcbp* mutants. Strikingly, in contrast to the radially organized symbiosomes around the central vacuole in the WT controls, we observed disorganized symbiosomes in symbiotic cells of *nkcbp* mutants (Supplementary Movies 3 and 5). Collectively, these results strongly suggested that nKCBP is required for vacuolar fusion during central vacuole morphogenesis by regulating the cytoskeletal organization during root nodule symbiosis.

KCBP genes in plants show functional conservation

We compared the sequence similarity and identity of KCBP in representative species, and found that KCBP proteins are highly conserved in different species, with identical domain organization (Supplementary Figs. 6 and 7). To further confirm the conservation of *KCBP* genes and clarify the specific contribution of various domains of nKCBP, we conducted a series of domain truncations nKCBP using a binary expression vector under the *L. japonicus* polyubiquitin (*Ljubq1*) promoter[42,43], separately. Then, the constructs were introduced into the *nkcbp* mutant through hairy-root transformation. The nodules were collected 3 weeks after rhizobial inoculation, and internal nodule structures were analysed by semi-thin sectioning. We firstly calculated the transformation-positive hairy roots and complementary events (Fig. 6a). Compared with the control *nkcbp* mutant expressing the empty vector, the *ProLjUb::MtnKCBP* and *ProLjUb::MtKCBP* constructs could complement the vacuole morphological defects of symbiotic cells in *nkcbp* mutants (Fig. 6b,c). Importantly, hairy roots expressing *ProLjUb::GmnKCBP*, one of the two *nKCBP* homologues in *G. max* (Glyma11G089400) and *ProLjUb::AtKCBP*, the only KCBP in *Arabidopsis*, could also rescue the vacuolar defects (Fig. 6d,e).

The highly conserved motor domain (containing ATP-hydrolysis and microtubule-binding sites) and FERM domain (linking actin cytoskeleton) are two featured domains in KCBP. We firstly introduced a point mutation of threonine 977 to asparagine in the conserved ATP-binding motif[21,24] of MtnKCBP to generate a rigor nKCBP variant, which binds microtubules but does not walk along microtubules. Notably, expressing the *ProLjUb::MtnKCBP-rigor* construct by hairy-root transformation in *nkcbp* mutants could not rescue the central vacuole defects in symbiotic cells (Fig. 6a,g), while the FERM domain (amino acids 275–499) deletion construct, *ProLjUb::MtnKCBP-ΔFERM*, could partially rescue the central vacuole defects, with a large proportion of uncomplemented events (Fig. 6a,h).

Collectively, we propose that the biochemical function of KCBPs should be conserved in the plant kingdom and *KCBP* genes undergo a duplication event. *nKCBP* acquires the nodulation-enriched expression with uncharacterized regulatory elements, and *nKCBP* is co-opted by rhizobia to regulate the rhizobia–legume symbiosis. nKCBP localizes to endoplasmic microtubules surrounding symbiosomes, and dynamically binds F-actin via the FERM domain to establish the required F-actin architecture, which ensures central vacuole formation by modulating membrane trafficking and vacuolar fusion during symbiosome development (see the model in Fig. 6i).

Discussion

Our findings uncovered a mechanism whereby the KCBP kinesin motor regulates vacuole morphogenesis in symbiotic cell differentiation during legume–rhizobia interaction. The demand for membrane trafficking activity is extremely high during the massive expansion of the symbiotic interface and extensive nutrient exchange between the symbiotic partners. nKCBP probably regulates vacuole morphogenesis in symbiotic cell differentiation by modulating membrane trafficking and vacuolar fusion.

Plant vacuoles are multi-functional organelles and participate in many cellular activities, such as building up the turgor pressure that drives cell wall expansion, material storage that maintains plant life[18,44,45]. In legume plants, vacuole morphogenesis is a key event during the adaptation between plants and intracellular symbiotic bacteria[19]. In particular, the colonization of thousands of symbiosomes within a single symbiotic cell requires the vacuole formation pathway and tonoplast-targeted trafficking[19]. From the apex to the base, the *Medicago* nodule is composed of persistent meristem zone (ZI), infection zone (ZII), interzone (IZ) and nitrogen-fixation zone (ZIII), which represent different developmental stages. Meristematic cells in the nodule meristem contain numerous, small vacuoles, which become larger during nodule cell differentiation. Once the nodule cells are colonized by rhizobia, vacuoles display remarkable changes including slower vacuole fusion, reduced vacuole volume proportion and blocked vacuole membrane folding, compared with those of the uninfected cells[19]. The differentiation of infected cells undergoes massive expansion and active remodelling of the endomembrane systems; therefore, we propose that nKCBP's regulation on cytoskeletal dynamics and vacuole fusion is extremely critical at this stage. Combing live-cell imaging with high-resolution electron microscopy, we have carefully examined the vacuole formation in different nodule zones. As expected, we observed clear differences in vacuole morphology between WT and the *nkcbp* mutant in infected cells. Moreover, we performed convincing genetic complementation experiments and

Fig. 4 | The *nkcbp* mutant shows defects of symbiosome development and bacteroid differentiation. a–**f**, Ultrastructures of nodules in the nitrogen-fixing zone of WT (**a**, **c** and **e**) and *nkcbp* mutants (**b**, **d** and **f**) at 14 dpi. ITs harbour the colonized rhizobia (**a** and **b**) in infected cells. In WT symbiotic cells, the central vacuole contains numerous defective rhizobia or undifferentiated bacteroids upon degradation (**c**), and well-developed symbiosomes are radially distributed around the central vacuole (**e**), while in *nkcbp*, small vacuoles are in symbiotic cells (**d**), which contain a large portion of incompletely differentiated symbiosomes, exhibiting dysplastic morphology, an enlarged peribacteroid space and disorganized symbiosome membrane (**f**). V, central vacuoles; FV, fragmented vacuole in infected *nkcbp* cells; red circles indicate abnormal differentiated bacteroids; red arrows mark the bacteria inside the infected threads; red asterisks indicate the bacteroids with dysplastic morphology; red arrowheads indicate abnormal symbiosome membrane. Nodules of SEM were randomly selected from 36 plants with at least three biological replicates. Scale bars, 2 μm (**a**–**f**). **g**, DNA content of DAPI-stained bacteroids from WT and *nkcbp* mutants measured by flow cytometry. The nodules used for flow cytometry were from at least 21 plants with three biological replicates. P1 represents the total signal counts excluding the cell debris. P2 represents the signal counts including just single bacteroid signals. P3 represents the bacteriod counts of the same area of WT and *nkcbp* mutants at lower fluorescence level. P4 represents the bacteriod counts of the same area of WT and *nkcbp* mutants at higher fluorescence level. WT: P1 = 25,487; P2 = 24,170; P3 = 2,458, P4 = 6,507; *nkcbp* mutant: P1 = 24,896; P2 = 24,591; P3 = 2,339, P4 = 5,281.

https://doi.org/10.1038/s41477-022-01261-4

revealed that, under the control of the constitutive promoter *ProLjUb*, *nKCBPs* and *KCBPs* of *Arabidopsis*, *Medicago* and soybean could rescue the vacuole defects in *nkcbp* mutants. Our findings strongly indicated that nKCBP-mediated central vacuole formation is essential for rhizobia colonization and symbiosome accommodation to ensure highly efficient nitrogen fixation.

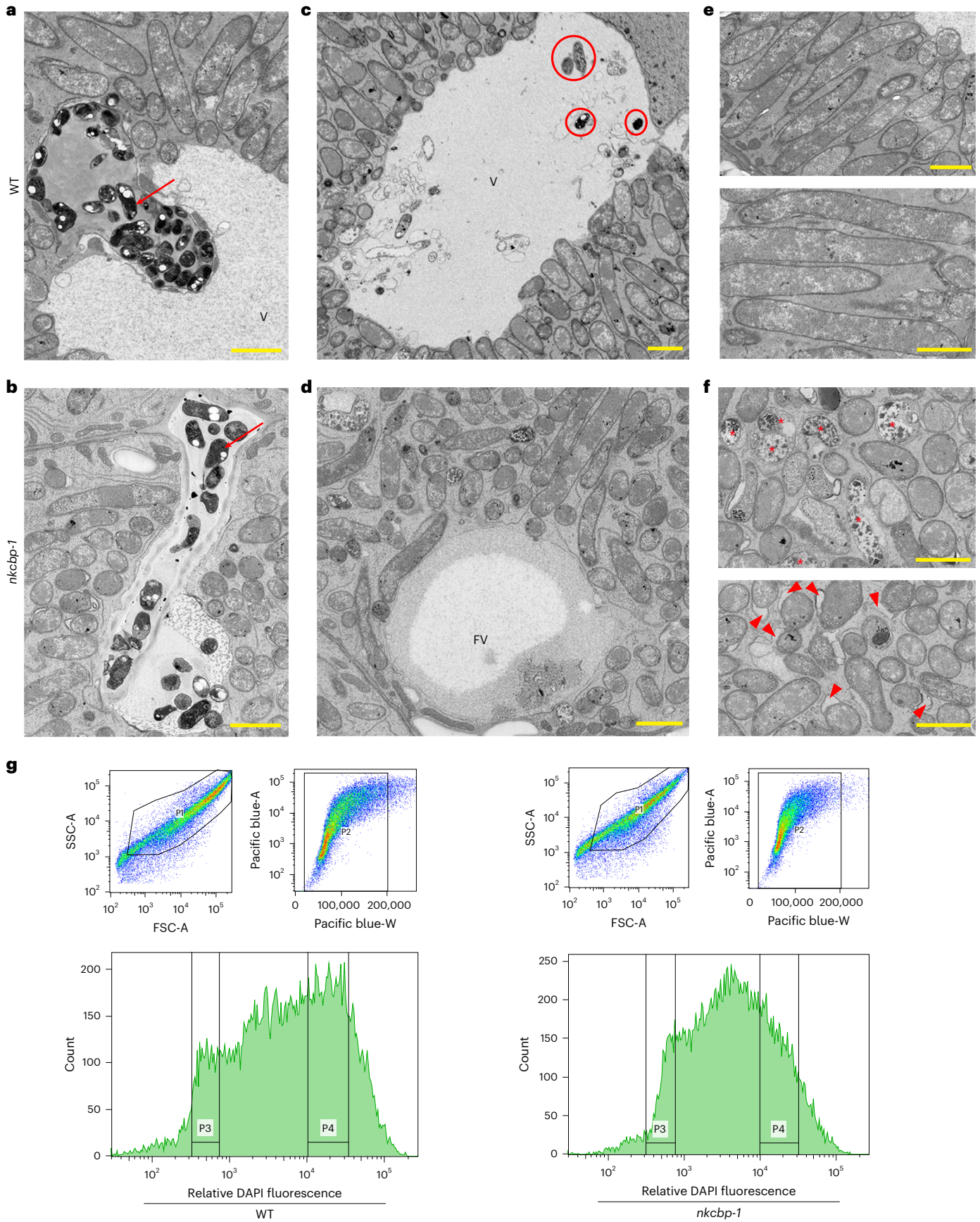

Microtubules and actin filaments do play pivotal roles during legume–rhizobia symbiosis[15–17] and in modulating vacuole morphologies and positioning[40,41,46,47]. Microtubules have been proved to play a critical role in the distribution of the vacuole in *Physcomitrella patens*[46]. In addition, KCBP has been shown to modulate the organization of microtubules and microfilaments to reposition the organelles and to disrupt the elongation in conifer pollen tubes[47]. In *nkcbp* mutants, both the microtubule cytoskeleton and the actin cytoskeleton displayed disordered organization and distribution patterns. One possibility is that microtubule-based nKCBP modulates F-actin dynamics via the FERM domain, and the interplay between microtubules and actin filaments dynamically modulates vacuole fusion and maturation via adaptors, which tether vacuolar vesicles. Another intriguing scenario is that vacuolar vesicles could be the cargo of the KCBP motor, and this notion is supported by recent in vitro reconstruction assays, which showed that *P. patens* KCBP directly binds to and transports membranous liposomes along microtubules, and that nuclear and chloroplasts are potential cargoes of this kinesin motor in vivo[48,49]. Most likely, both of these scenarios co-exist during symbiosome development. Therefore, loss of *nKCBP* function disturbs cytoskeletal dynamics, thus disrupting membrane trafficking and central vacuole formation. Central vacuole deficiency in *nkcbp* nodules impairs infected cell differentiation and rhizobia accommodation, ultimately abolishing nitrogen fixation. Most convincingly, our complementation experiments using motor-dead and FERM (the actin-binding domain)-deficiency versions clearly indicated that both microtubule- and actin-related functions of nKCBP are required for central vacuole formation in symbiotic cells.

Importantly, our findings further reveal that duplication of KCBP-encoding genes occurred solely in legumes that form the more advanced symbiotic form, symbiosomes, but did not occur in the species that form the primitive symbiotic organ, fixation threads. These findings indicated a coincidence between co-option of the duplicated *KCBP* by rhizobia and the emergence of symbiosomes, suggesting an important role of nKCBP in symbiosome formation. The emergence of symbiosomes represents a major step and an advanced evolutionary event[34]. Hence, *KCBP* duplication has allowed functional specialization of the resulting paralogous *nKCBP* for symbiosome development, while the other copy has retained the molecular and biochemical functions of KCBP that are probably conserved from algae to higher plants[22]. It will be important to investigate which genetic events changed the expression pattern and the regulation of the duplicated legume *KCBPs*, which were then co-opted by rhizobia for symbiotic cell differentiation and symbiosome accommodation. Further investigation is also required to identify genes that co-evolved with *nKCBP* to form a regulatory network for symbiotic accommodation. Candidates would be genes encoding components of the ARP2/3 actin nucleation complex. Previous work showed that ARP3, one of the components of the ARP2/3 actin nucleation complex, is required for vacuole formation in trichomes in *Arabidopsis*[40]. In addition, knockdown of *ARP3* in *M. truncatula* results in defects of central vacuole formation and symbiosome maturation[16]. Previous studies reported that KCBP acts in the same genetic pathway with ARP3 and SCAR2, a subunit of the W/SRC complex, the activator of the ARP2/3 complex[50–52]. Partial complementation capability of the FERM-deletion version of nKCBP also revealed that FERM-mediated actin-binding function of nKCBP might share redundant functions with other actin-related proteins. In conclusion, our findings shed light on cellular mechanisms of root nodule symbiosis, and provide important insights into methods for crop yield improvement and sustainable agriculture.

Methods

Plant materials and bacterial strains

M. truncatula ecotype A17 and R108 were used in our experiments. *S. meliloti* strain 2011 (Sm2011) (refs. [53,54]) was used to inoculate *M. truncatula* roots to form symbiotic nodules. *Agrobacterium rhizogenes* strain MSU440 was used for hairy-root transformation in *M. truncatula*. *Agrobacterium tumefaciens* strain EHA105 was used for stable transformation of *M. truncatula*, and for *N. benthamiana* transient expression. Plant growth conditions and rhizobia inoculation were performed as previously described[15]. Root nodules were collected 4–28 dpi for various assays.

Phylogenetic analysis

The protein sequences of KCBPs from 26 species were obtained from Phytozome 10.1 (http://phytozome.jgi.doe.gov/pz/portal.html) and the National Center for Biotechnology Information (NCBI; https://blast.ncbi.nlm.nih.gov/Blast.cgi), and the *L. japonicus* KCBP sequence was obtained from http://www.kazusa.or.jp/lotus/blast.html. Protein sequences were aligned using ClustalW, and the phylogenetic tree was generated using the neighbour-joining method of MEGA5.0. The bootstrapping value was set at 1,000 replications to evaluate the consistency of the analysis.

Plasmid construction

As described in the previous study[15,55], the Phusion DNA polymerase with high fidelity (New England Biolabs) was used to amplify the full-length complementary DNA of nKCBP (primers: GFP-nKCBP-F and CDS-nKCBP-R), the FERM domain (primers: GFP-FERM-F and FERM-R) and green fluorescent protein (GFP; primers: GFP-F, GFP-nKCBP-R and GFP-FERM-R) fragments. Fusion PCR was applied to get the final GFP-nKCBP and GFP-FERM fusion fragments, and the Gateway-based technology was applied to obtain the final expression construct. To obtain the *pCambia1381- Pro$_{nKCBP}$* construct, we used ClonExpress II One Step Cloning Kit (Vazyme) to ligate the *Pro$_{nKCBP}$* fragment (1381-Pro-F and 1381-Pro-R), and PstI/SalI-linearized *pCambia1381* binary vector. For the complementation constructs *pUB-MtnKCBP*, *pUB-GmnKCBP*, *pUB-MtKCBP*, *pUB-AtKCBP*, *pUB-MtnKCBP-rigor* and *pUB-MtnKCBP-ΔFERM*, we used ClonExpress II One Step Cloning Kit (Vazyme) to ligate target fragments and KpnI/XbaI-linearized *pUB-GFP* binary vector. (*MtnKCBP*: pUB-MtnKCBP-F and pUB-MtnKCBP-R; *GmnKCBP*: pUB-GmnKCBP-F and pUB-GmnKCBP-R; *MtKCBP*: pUB-MtKCBP-F and pUB-MtKCBP-R; *AtKCBP*: pUB-AtKCBP-F and pUB-AtKCBP-R; *MtnKCBP-rigor*: pUB-MtnKCBP-rigor-F, pUB-MtnKCBP-rigor-M-R; pUB-MtnKCBP-rigor-M-F and pUB-MtnKCBP-rigor-R; *MtnKCBP-ΔFERM*: pUB-MtnKCBP-ΔFERM-F, pUB-MtnKCBP-ΔFERM-M-R; pUB-MtnKCBP-ΔFERM-M-F and pUB-MtnKCBP-ΔFERM-R). The sequences of the above-mentioned primers are listed in Supplementary Table 1.

Fig. 5 | Localization of nKCBP and cytoskeletal organization in symbiotic cells. a, *M. truncatula* nKCBP was fused to the C-terminus GFP and expressed under the control of its native promoter in a stable transgenic line. Sm2011-RFP was used for infection. Yellow arrowheads indicate ITs. In infected cells, nKCBP signals display linear punctate, with some particles closely associated with symbiosome membrane and others in peri-symbiont space. Insets show that linear vesicle-like particles are aligned with symbiosomes. **b**, Co-localization of nKCBP (anti-GFP-FITC) with microtubules (anti-α-tubulin-TRITC) in infected cells. nKCBP particles display linear punctate along microtubules. **c**, Co-localization of nKCBP-GFP with actin (TRITC–phalloidin) in infected cells. Only a small portion of nKCBP particles localize on actin filaments. **d**, Endoplasmic microtubules are oriented mainly parallel to symbiosomes radially around central vacuole in infected cells of the WT control, but are disordered in infected cells of the *nkcbp* mutant. **e**, Actin filaments are aligned towards the central vacuole in WT infected cells, but are randomly distributed in infected cells of the *nkcbp* mutant. The nodules for confocal observation were collected from at least 36 plants with three biological replicates. Scale bars, 25 μm (**a**), 20 μm (**b**), 10 μm (**c**) and 20 μm (**d** and **e**).

https://doi.org/10.1038/s41477-022-01261-4

CRISPR/Cas9-mediated genome editing

To knock out the *nKCBP* (Medtr5g025100), we employed the CRISPR/Cas9-mediated genome editing technology[56,57]. Firstly, we modified the expressing vector of *pCambia1300-pYAO::Cas9* (ref. [57]). and replaced the *YAO* promoter with the promoter of *Arabidopsis Ubiquitin10* (refs. [15,58]) to optimize the transformation in *M. truncatula*. Then, a

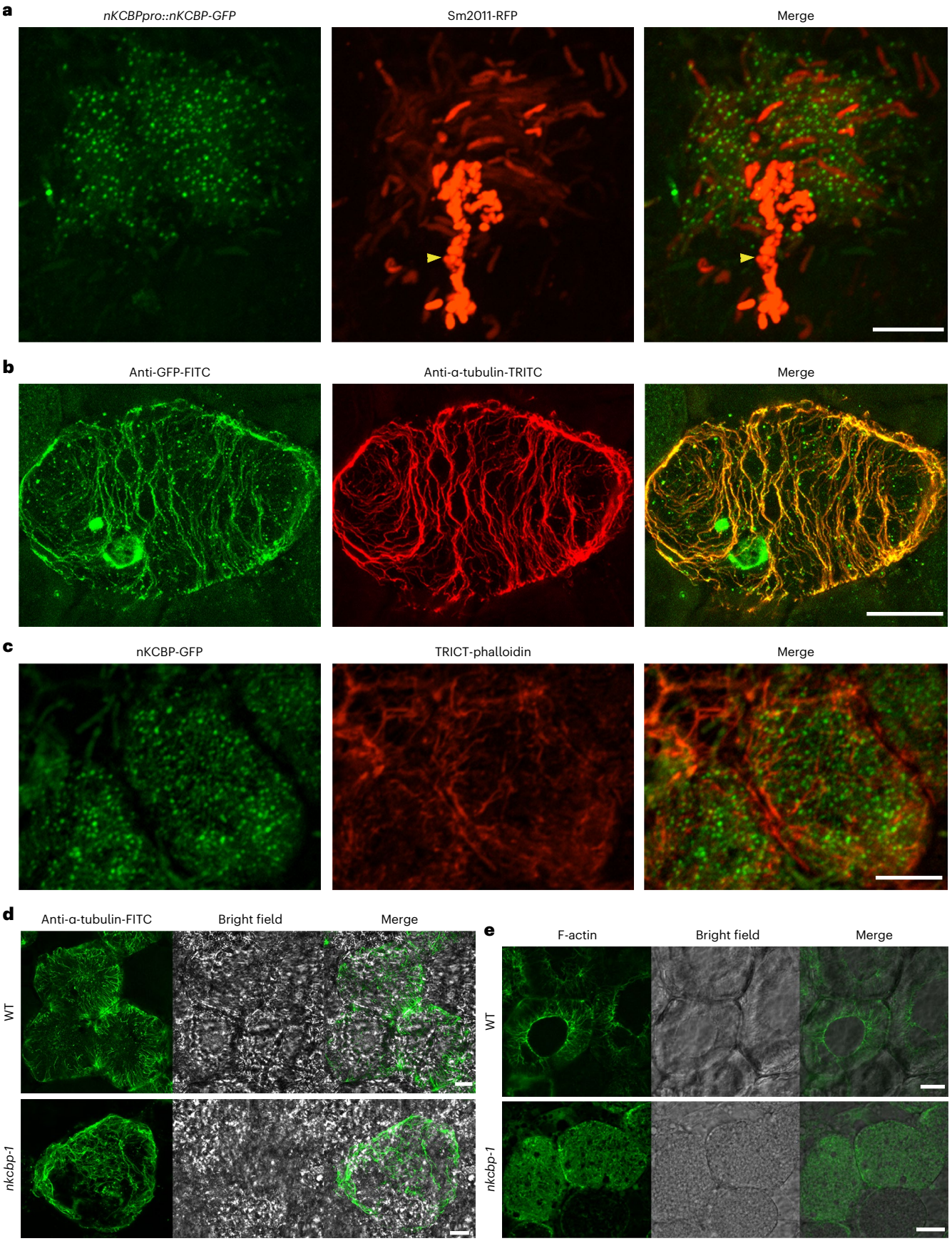

https://doi.org/10.1038/s41477-022-01261-4

a

Constructs	Complementary roots/total positive roots
Empty vector	0/24
ProLjUb::MtnKCBP	30/36
ProLjUb::GmnKCBP	26/31
ProLjUb:: MtKCBP	28/40
ProLjUb:: AtKCBP	47/79
ProLjUb::MtnKCBP-rigor	0/51
ProLjUb::MtnKCBP-ΔFERM	9/79

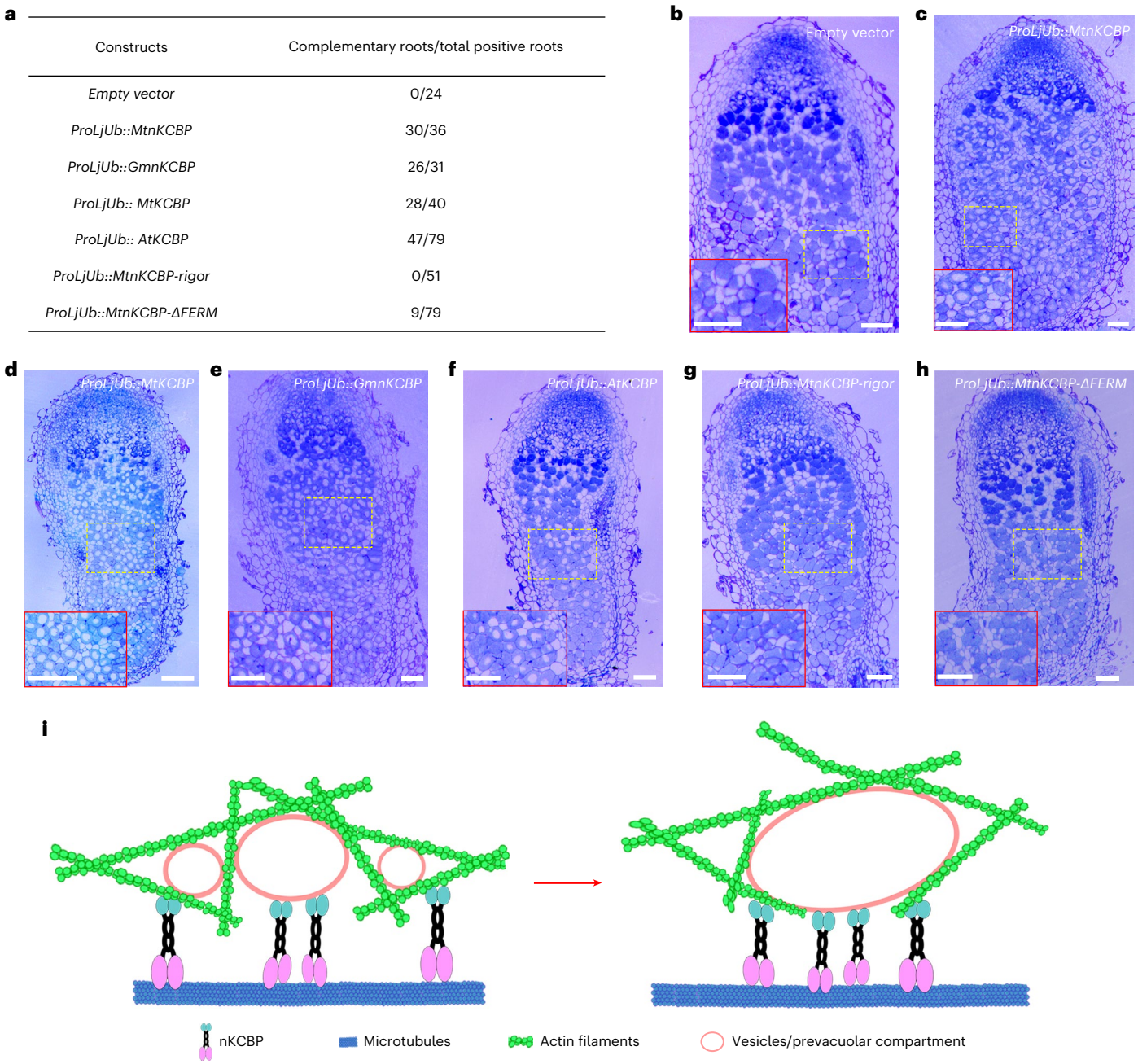

Fig. 6 | nKCBP regulates cytoskeletal organization to control central vacuole formation during symbiotic nodule development. a, KCBPs from different species have conserved biochemical properties, and function of nKCBP in central vacuole formation is both microtubule dependent and actin dependent. Complementary analysis of *KCBP* genes from *Medicago*, soybean and *Arabidopsis*, and nKCBP variants of defective microtubule (T977N) and actin function (deletion of amino acids 275–499). Constructs were introduced in *nkcbp* mutant plants by hairy-root transformation. GFP expressed from the construct was used as a selection marker for transformations and positive nodules were selected at 21 dpi. For all plants, at least two biological replicates were performed. **b**–**h**, Representative images of semi-thin nodule sections transformed with empty vector (**b**), *ProLjUb::MtnKCBP* (**c**), *ProLjUb::MtKCBP* (**d**), *ProLjUb::GmnKCBP* (**e**), *ProLjUb::AtKCBP* (**f**), *ProLjUb::MtnKCBP-rigor* (**g**) and *ProLjUb::MtnKCBP-ΔFERM* (**h**). The lower left images are a close-up view of the yellow dashed rectangles. For all plants, at least two biological replicates were performed. **i**, The working model of nKCBP in central vacuole formation in symbiotic cells: microtubule-based nKCBP dynamically binds F-actin to establish the required F-actin architecture for central vacuole morphogenesis. nKCBP regulates small vacuolar vesicle fusion (left) to form the large central vacuole (right) either via F-actin or by directly binding to vacuolar vesicles. Scale bars, 0.1 mm (**b**–**h**).

single guide RNA site (GGTGATGGATATGACAGTGA) was designed. Two DNA oligos CRISPR-nKCBP-F/CRISPR-nKCBP-R were synthesized and annealed. The *pCAMBIA1300-ProAtUbq10::Cas9-nKCBP* construct was obtained as described in the previous study[56]. The target construct was introduced into *A. tumefaciens* strain EHA105 by electroporation, and *Agrobacterium*-mediated transformation of *M. truncatula* was performed as described previously[15,56]. The *nkcbp* lines were screened by PCR with primers nKCBP(test)-F/nKCBP(test)-R, and confirmed by sequencing[59]. The sequences of the above-mentioned primers are listed in Supplementary Table 1.

nKCBP subcellular location in *N. benthamiana*

The expression vectors of *35S::GFP-nKCBP* and *mCherry-TUB6* (labelling microtubule) were co-expressed in *N. benthamiana* to observe the co-localization between nKCBP and microtubules. The expression vectors of *35S::GFP-FERM* and *ABD2-mCherry* (labelling F-actin) were co-expressed in *N. benthamiana* to observe the co-localization between the FERM domain of nKCBP and F-actin. Leaves were detached and used for image acquisition 2 days after infiltration.

Acetylene reduction assay

The *M. truncatula* seedlings were grown on vermiculite and inoculated with Sm2011. Nodules at 28 dpi were collected and put into a closed 20 ml vial containing 2 ml acetylene (C_2H_2) at 28 °C for 3 h (refs. [60,61]). For each sample, three biological replicates were performed for analysis. Acetylene was measured using a GC-4000A gas chromatograph.

Complementation experiments

A. rhizogenes-mediated hairy-root transformation was conducted as described in our previous study[15,56]. All the complementary constructs and the empty vector pUB-GFP were introduced into the *A. rhizogenes*. After 7 days of co-cultivation of *nkcbp* mutants with *A. rhizogenes* carrying proper complementation constructs, hairy roots were induced for 2 weeks. GFP-positive roots were selected after infection with rhizobia for 3 weeks. Positive nodules were collected for semi-section. At least 24 positive roots of *nkcbp* mutants were analysed for each construct. Two independent replicates were performed for each construct.

Real-time PCR

Total RNA was extracted from *Medicago* roots, stems, leaves, flowers, nodules and pods using the Rapid EASYspin plant RNA extraction kit (Biomed). Two micrograms of total RNA for each sample was applied for reverse transcription using the SuperScript III First-Strand Synthesis System (Invitrogen) with oligo (dT) primers. Real-time RT–PCR was conducted using the SYBR Green Realtime PCR Master Mix (TOYOBO). The PCR amplification reactions were performed as described previously[56]. *MtACTIN11* was used as the reference gene (MtACTIN11-F/MtACTIN11-R)[62]. nKCBP-F and nKCBP-R were primers of *nKCBP* for RT–PCR. All reactions were performed in triplicate. Primers for RT-PCR are listed in Supplementary Table 1.

Staining analysis

For GUS staining: nodules of hairy roots were collected at 7 and 14 dpi, respectively, and stained for GUS activity for about 6 h. For semi-thin sections, the nodules were cut into sections (thickness, 10 µm) with a Leica RM2265 microtome, stained with 0.1% Ruthenium Red[56,63] (Sigma-Aldrich) and analysed using a Leica M205FA microscope equipped with a DFC450c camera (Leica). For toluidine blue staining: the staining was performed as described previously[15]. For F-actin staining: the hand-cut nodule sections (expressed nKCBP-GFP) were incubated with phalloidin (Thermo Fisher Scientific), dilution 1:100 in fluorescence buffer (10 mM imidazole, pH 7.0; 50 mM KCl; 2 mM $MgCl_2$; 1 mM EGTA;100 mM dithiothreitol; 100 µg ml^{-1} glucose oxidase; 15 mg ml^{-1} glucose; 20 mg ml^{-1} catalase and 0.5% methylcellulose)[15,64].

Immunofluorescence experiment

Nodule manual sections were fixed in 1% (w/v) freshly depolymerized paraformaldehyde in PBS (pH 7.0) for 30 min, and then were blocked in goat serum for 30 min. The sections were further incubated with the primary antibody overnight at 4 °C in PBS containing 0.05% (v/v) Triton X-100 at 1:100 dilution[65]. The secondary antibody conjugated with FITC/TRITC, was diluted at 1:50. For immunofluorescence, the primary antibody is anti-α-tubulin from rabbit and the secondary antibody is goat-anti-rabbit conjugated with FITC.

For double immunofluorescence, the primary antibodies are anti-α-tubulin from mouse and anti-GFP from rabbit, the secondary antibodies are goat-anti-rabbit conjugated with FITC and goat-anti-mouse conjugated with TRITC. Non-GFP control (WT) nodules were used as the negative control.

Sample preparations for SEM

Nodules at 14 dpi were incubated in phosphate buffer (0.1 M, pH 7.4) with 2.5% (vol/vol) glutaraldehyde, and were subsequently rinsed four times with phosphate buffer. Then they were first immersed in 1% (w/v) OsO_4 and 1.5% (w/v) potassium ferricyanide aqueous solution at 4 °C for 1 h. After washing, the nodules were incubated in filtered 1% thiocarbohydrazide aqueous solution (Sigma-Aldrich) at room temperature for 30 min, 1% unbuffered OsO_4 aqueous solution at 4 °C for 1 h and 1% uranyl acetate aqueous solution at 4 °C overnight following four rinses in ddH_2O for 10 min each between each step. Following dehydration in an acetone series (30%, 50%, 70%, 80%, 90%, 100%, 100%, 10 min each at 4 °C), the nodules were dehydrated by pure acetone (3 × 10 min). Nodules were infiltrated in graded mixtures (3:1, 1:1 and 1:3) of acetone and SPI-PON812 resin (19.6 ml SPI-PON812, 6.6 ml dodecenyl succinic anhydride and 13.8 ml nadic methyl anhydride and 1.5% dimethylbenzylamine), then in pure resin. Finally, nodules were embedded in pure resin with 1.5% dimethylbenzylamine and polymerized for 12 h at 45 °C, 48 h at 60 °C.

High-resolution images (accelerating voltage of 2 kV, beam current of 0.69 nA, pixel size of 15 nm, dwell time of 10 µs) were acquired by concentric backscattered detector of scanning electron microscope FEI Helios NanoLab 600i.

AutoCUTS-SEM

Serial sections for 3D reconstruction of symbiotic cells were obtained by AutoCUTS[37]. The nodule resin blocks were prepared and the automatic collection of serial nodule sections was accomplished by AutoCUTS device (100 nm each section, 1,000 sections). Then the wafer was observed using scanning electron microscope FEI Helios NanoLab 600i. To gain the precise SEM coordinates of nodules for high-resolution imaging, low-resolution images (accelerating voltage of 2 kV, beam current of 0.34 nA, pixel size of 184 nm, dwell time of 3 µs) were acquired by CBS detector in a field-free low-magnification mode using the FEI iFast software. High-resolution images were finally automatically acquired by CBS detector in an immersion high-magnification mode using the FEI iFast software with the parameters including accelerating voltage of 2 kV, beam current of 0.34 nA, pixel size of 15 nm and dwell time of 10 µs. This process was repeated for each section on a wafer, then on each wafer in the section library. Finally, the serial images acquired with AutoCUTS-SEM were corrected and aligned before 3D reconstruction using MiRA-Align. All datasets were analysed using Imaris 9.2.1 software. Structures of cell wall, nucleus and vacuole were manually traced and segmented for 3D reconstruction.

Sample preparation and flow cytometry assays. Nodules of WT and *nkcbp* mutants were collected and sliced in 0.5 ml of Galbraith buffer containing 1% Triton X-100, nuclei were stained with DAPI (5 µg ml^{-1}) (ref. [66]). In the case of bacteria, 30,000 bacteroids were analysed. DNA content of bacteria was measured with flow cytometry (BD FACSCalibur) driven by FACSDiva Version 6.1.3 software.

Confocal microscopy and image analysis

Nikon A1 confocal microscopy equipped with five laser wavelengths was used for immunofluorescence analysis. TRITC was excited at 561 nm, and FITC was excited at 488 nm. Other images were carried out under a spinning disk confocal microscope (UltraView VoX, PerkinElmer) equipped with the Yokogawa Nipkow CSU-X1 spinning disk scanner, Hamamatsu EMCCD 9100-13, Nikon TiE inverted microscope with the Perfect Focus System. RFP, mCherry and neutral red were excited at 561 nm. GFP was excited at 488 nm. Acquired images were processed and analysed using software of Volocity (PerkinElmer), ImageJ (http://rsbweb.nih.gov/ij), as described previously[15,24,55].

To observe the F-actin and vacuoles in WT/*nkcbp* nodule cells, we used *A. rhizogenes*-mediated hairy-root transformation to introduce appropriate vectors (*ProAtUbq10::ABD2-GFP* for F-actin, *ProAtUbq10::mCherry-VAMP711* for vacuoles). Nodules were collected 10–21 dpi for experiments. Hand sections were made and observed by spinning disk confocal microscope.

Quantification and statistical analysis

All statistical details (statistical test used and *P* values) for the experiment can be found in the figure legends.

Reporting summary

Further information on research design is available in the Nature Research Reporting Summary linked to this article.

Data availability

All data generated in this study are included within the main text and supplementary information. The *MtnKCBP* gene can be found at Phytozome (https://phytozome-next.jgi.doe.gov/report/gene/Mtruncatula_Mt4_0v1/Medtr5g025100). Protein sequences in Fig. 1d for the phylogenetic analysis and in Supplementary Fig. 6 for the pairwise sequence alignment are accessible either at NCBI (https://blast.ncbi.nlm.nih.gov/Blast.cgi) or at Phytozome (https://phytozome-next.jgi.doe.gov/), with gene IDs provided in Fig. 1d and Supplementary Fig. 6 legends. All experimental materials generated in this work are available from the corresponding author upon request. Source data are provided with this paper.

References

1. Martin, F. M., Uroz, S. & Barker, D. G. Ancestral alliances: plant mutualistic symbioses with fungi and bacteria. *Science* **356**, aad450 (2017).
2. Suzaki, T., Yoro, E. & Kawaguchi, M. Leguminous plants: inventors of root nodules to accommodate symbiotic bacteria. *Int. Rev. Cel. Mol. Bio.* **316**, 111–158 (2015).
3. Xiao, T. T. et al. Fate map of *Medicago truncatula* root nodules. *Development* **141**, 3517–3528 (2014).
4. Franssen, H. J. et al. Root developmental programs shape the *Medicago truncatula* nodule meristem. *Development* **142**, 2941–2950 (2015).
5. Roy, S. et al. Celebrating 20 years of genetic discoveries in legume nodulation and symbiotic nitrogen fixation. *Plant Cell* **32**, 15–41 (2020).
6. Oldroyd, G. E., Murray, J. D., Poole, P. S. & Downie, J. A. The rules of engagement in the legume-rhizobial symbiosis. *Annu. Rev. Genet.* **45**, 519–546 (2011).
7. Oldroyd, G. E. & Downie, J. A. Coordinating nodule morphogenesis with rhizobial infection in legumes. *Annu. Rev. Plant Biol.* **59**, 519–546 (2008).
8. Desbrosses, G. J. & Stougaard, J. Root nodulation: a paradigm for how plant–microbe symbiosis influences host developmental pathways. *Cell Host Microbe* **10**, 348–358 (2011).
9. Ferguson, B. J. et al. Molecular analysis of legume nodule development and autoregulation. *J. Integr. Plant Biol.* **52**, 61–76 (2010).
10. Gavrin, A. et al. VAMP721a and VAMP721d are important for pectin dynamics and release of bacteria in soybean nodules. *N. Phytol.* **210**, 1011–1021 (2016).
11. Jayaraman, D., Gilroy, S. & Ane, J. M. Staying in touch: mechanical signals in plant–microbe interactions. *Curr. Opin. Plant Biol.* **20**, 104–109 (2014).
12. Gavrin, A., Kulikova, O., Bisseling, T. & Fedorova, E. E. Interface symbiotic membrane formation in root nodules of *Medicago truncatula*: the role of synaptotagmins *MtSyt1*, *MtSyt2* and *MtSyt3*. *Front. Plant Sci.* **8**, 201–210 (2017).
13. Brandizzi, F. & Wasteneys, G. O. Cytoskeleton-dependent endomembrane organization in plant cells: an emerging role for microtubules. *Plant J.* **75**, 339–349 (2013).
14. Mathur, J. & Hulskamp, M. Microtubules and microfilaments in cell morphogenesis in higher plants. *Curr. Biol.* **12**, R669–R676 (2002).
15. Zhang, X. X. et al. The host actin cytoskeleton channels rhizobia release and facilitates symbiosome accommodation during nodulation in *Medicago truncatula*. *N. Phytol.* **221**, 1049–1059 (2018).
16. Gavrin, A., Jansen, V., Ivanov, S., Bisseling, T. & Fedorova, E. ARP2/3-mediated actin nucleation associated with symbiosome membrane is essential for the development of symbiosomes in infected cells of *Medicago truncatula* root nodules. *Mol. Plant Microbe Interact.* **28**, 605–614 (2015).
17. Kitaeva, A. B., Demchenko, K. N., Tikhonovich, I. A., Timmers, A. C. & Tsyganov, V. E. Comparative analysis of the tubulin cytoskeleton organization in nodules of *Medicago truncatula* and *Pisum sativum*: bacterial release and bacteroid positioning correlate with characteristic microtubule rearrangements. *N. Phytol.* **210**, 168–183 (2016).
18. Zhang, C., Hicks, G. R. & Raikhel, N. V. Plant vacuole morphology and vacuolar trafficking. *Front. Plant Sci.* **5**, 476 (2014).
19. Gavrin, A. et al. Adjustment of host cells for accommodation of symbiotic bacteria: vacuole defunctionalization, HOPS suppression, and TIP1g retargeting in *Medicago*. *Plant Cell* **26**, 3809–3822 (2014).
20. Parniske, M. Uptake of bacteria into living plant cells, the unifying and distinct feature of the nitrogen-fixing root nodule symbiosis. *Curr. Opin. Plant Biol.* **44**, 164–174 (2018).
21. Reddy, V. S. & Reddy, A. S. N. A plant calmodulin-binding motor is part kinesin and part myosin. *Bioinformatics* **15**, 1055–1057 (1999).
22. Abdel-Ghany, S. E., Day, I. S., Simmons, M. P., Kugrens, P. & Reddy, A. S. N. Origin and evolution of kinesin-like calmodulin-binding protein. *Plant Physiol.* **138**, 1711–1722 (2005).
23. Reddy, A. S. N., Safadi, F., Narasimhulu, S. B., Golovkin, M. & Hu, X. A novel plant calmodulin-binding protein with a kinesin heavy chain motor domain. *J. Biol. Chem.* **271**, 7052–7060 (1996).
24. Tian, J. et al. Orchestration of microtubules and the actin cytoskeleton in trichome cell shape determination by a plant-unique kinesin. *eLife* **4**, e09351 (2015).
25. Rensing, S. A. Plant Evo-Devo: how tip growth evolved. *Curr. Biol.* **26**, R1228–R1230 (2016).
26. Honkanen, S. et al. The mechanism forming the cell surface of tip-growing rooting cells is conserved among land plants. *Curr. Biol.* **26**, 3238–3244 (2016).
27. Breakspear, A. et al. The root hair 'infectome' of *Medicago truncatula* uncovers changes in cell cycle genes and reveals a requirement for auxin signaling in rhizobial infection. *Plant Cell* **26**, 4680–4701 (2014).
28. Carrere, S., Verdier, J. & Gamas, P. MtExpress, a comprehensive and curated RNAseq-based gene expression atlas for the model legume *Medicago truncatula*. *Plant Cell Physiol.* **62**, 1494–1500 (2021).
29. Zhang, T. et al. Sequencing of allotetraploid cotton (*Gossypium hirsutum* L. acc. TM-1) provides a resource for fiber improvement. *Nat. Biotechnol.* **33**, 531–537 (2015).
30. Bolsheva, N. L. et al. Evolution of blue-flowered species of genus *Linum* based on high-throughput sequencing of ribosomal RNA genes. *BMC Evol. Biol.* **17**, 253 (2017).
31. Dai, X. et al. The willow genome and divergent evolution from poplar after the common genome duplication. *Cell Res.* **24**, 1274–1277 (2014).
32. Schmutz, J. et al. Genome sequence of the palaeopolyploid soybean. *Nature* **463**, 178–183 (2010).

33. Behm, J. E., Geurts, R. & Kiers, E. T. Parasponia: a novel system for studying mutualism stability. *Trends Plant Sci.* **19**, 757–763 (2014).
34. Limpens, E. et al. Formation of organelle-like N_2-fixing symbiosomes in legume root nodules is controlled by *DMI2*. *Proc. Natl Acad. Sci. USA* **102**, 10375–10380 (2005).
35. Jauh, G. Y., Phillips, T. E. & Rogers, J. C. Tonoplast intrinsic protein isoforms as markers for vacuolar functions. *Plant Cell* **11**, 1867–1882 (1999).
36. Cui, Y. et al. A whole-cell electron tomography model of vacuole biogenesis in *Arabidopsis* root cells. *Nat. Plants* **5**, 95–105 (2019).
37. Li, X. X. et al. Large scale three-dimensional reconstruction of an entire *Caenorhabditis elegans* larva using AutoCUTS-SEM. *J. Struct. Biol.* **200**, 87–96 (2017).
38. Mathur, J. Mutations in actin-related proteins 2 and 3 affect cell shape development in *Arabidopsis*. *Plant Cell* **15**, 1632–1645 (2003).
39. Onelli, E. et al. Microtubules play a role in trafficking prevacuolar compartments to vacuoles in tobacco pollen tubes. *Open Biol.* **8**, 180078 (2018).
40. Wang, P., Hawkins, T. J. & Hussey, P. J. Connecting membranes to the actin cytoskeleton. *Curr. Opin. Plant Biol.* **40**, 71–76 (2017).
41. Scheuring, D. et al. Actin-dependent vacuolar occupancy of the cell determines auxin-induced growth repression. *Proc. Natl Acad. Sci. USA* **113**, 452–457 (2016).
42. Maekawa, T. et al. Polyubiquitin promoter-based binary vectors for overexpression and gene silencing in *Lotus japonicus*. *Mol. Plant Microbe Interact.* **21**, 375–382 (2008).
43. Qiu, L. P. et al. SCARN a novel class of SCAR protein that is required for root-hair infection during legume nodulation. *PLoS Genet.* **11**, e1005623 (2015).
44. Kruger, F. & Schumacher, K. Pumping up the volume—vacuole biogenesis in *Arabidopsis thaliana*. *Semin. Cell Dev. Biol.* **80**, 106–112 (2018).
45. Zouhar, J. & Rojo, E. Plant vacuoles: where did they come from and where are they heading? *Curr. Opin. Plant Biol.* **12**, 677–684 (2009).
46. Oda, Y. et al. Microtubules regulate dynamic organization of vacuoles in *Physcomitrella patens*. *Plant Cell Physiol.* **50**, 855–868 (2009).
47. Lazzaro, M. D., Marom, E. Y. & Reddy, A. S. N. Polarized cell growth, organelle motility, and cytoskeletal organization in conifer pollen tube tips are regulated by KCBP, the calmodulin-binding kinesin. *Planta* **238**, 587–597 (2013).
48. Yamada, M., Tanaka-Takiguchi, Y., Hayashi, M., Nishina, M. & Goshima, G. Multiple kinesin-14 family members drive microtubule minus end-directed transport in plant cells. *J. Cell Biol.* **216**, 1705–1714 (2017).
49. Jonsson, E., Yamada, M., Vale, R. D. & Goshima, G. Clustering of a kinesin-14 motor enables processive retrograde microtubule-based transport in plants. *Nat. Plants* **1**, 15087 (2015).
50. Schwab, B. et al. Regulation of cell expansion by the *DISTORTED* genes in *Arabidopsis thaliana*: actin controls the spatial organization of microtubules. *Mol. Gen. Genet.* **269**, 350–360 (2003).
51. Zhang, X., Grey, P. H., Krishnakumar, S. & Oppenheimer, D. G. The *IRREGULAR TRICHOME BRANCH* loci regulate trichome elongation in *Arabidopsis*. *Plant Cell Physiol.* **46**, 1549–1560 (2005).
52. Zhang, X., Dyachok, J., Krishnakumar, S., Smith, L. G. & Oppenheimer, D. G. *IRREGULAR TRICHOME BRANCH1* in *Arabidopsis* encodes a plant homolog of the actin-related protein2/3 complex activator Scar/WAVE that regulates actin and microtubule organization. *Plant Cell* **17**, 2314–2326 (2005).
53. Smit, P. et al. NSP1 of the GRAS protein family is essential for rhizobial Nod factor-induced transcription. *Science* **308**, 1789–1791 (2005).
54. Liu, W. et al. Strigolactone biosynthesis in *Medicago truncatula* and rice requires the symbiotic GRAS-type transcription factors NSP1 and NSP2. *Plant Cell* **23**, 3853–3865 (2011).
55. Liu, T. et al. Augmin triggers microtubule-dependent microtubule nucleation in interphase plant cells. *Curr. Biol.* **24**, 2708–2713 (2014).
56. Wang, Q. et al. Transfer cells mediate nitrate uptake to control root nodule symbiosis. *Nat. Plants* **6**, 800–808 (2020).
57. Yan, L. et al. High-efficiency genome editing in *Arabidopsis* using *YAO* promoter-driven CRISPR/Cas9 system. *Mol. Plant* **8**, 1820–1823 (2015).
58. Grefen, C. et al. A ubiquitin-10 promoter-based vector set for fluorescent protein tagging facilitates temporal stability and native protein distribution in transient and stable expression studies. *Plant J.* **64**, 355–365 (2010).
59. Wang, C. et al. KTN80 confers precision to microtubule severing by specific targeting of katanin complexes in plant cells. *EMBO J.* **36**, 3435–3447 (2017).
60. Wang, J. et al. A purple acid phosphatase plays a role in nodule formation and nitrogen fixation in *Astragalus sinicus*. *Plant Mol. Biol.* **88**, 515–529 (2015).
61. Lei, L. et al. A nodule-specific lipid transfer protein AsE246 participates in transport of plant-synthesized lipids to symbiosome membrane and is essential for nodule organogenesis in Chinese milk vetch. *Plant Physiol.* **164**, 1045–1058 (2014).
62. Gonzalez-Rizzo, S., Crespi, M. & Frugier, F. The *Medicago truncatula* CRE1 cytokinin receptor regulates lateral root development and early symbiotic interaction with *Sinorhizobium meliloti*. *Plant Cell* **18**, 2680–2693 (2006).
63. Wang, C. et al. *NODULES WITH ACTIVATED DEFENSE 1* is required for maintenance of rhizobial endosymbiosis in *Medicago truncatula*. *N. Phytol.* **212**, 176–191 (2016).
64. Han, L. B. et al. The two domains of cotton WLIM1a protein are functionally divergent. *Sci. China Life Sci.* **59**, 206–212 (2016).
65. Si, Z. Y. et al. Digalactosyldiacylglycerol synthase gene *MtDGD1* plays an essential role in nodule development and nitrogen fixation. *Mol. Plant Microbe Interact.* **32**, 1196–1209 (2019).
66. Sinharoy, S. et al. The C_2H_2 transcription factor regulator of symbiosome differentiation represses transcription of the secretory pathway gene *VAMP721a* and promotes symbiosome development in *Medicago truncatula*. *Plant Cell* **25**, 3584–3601 (2013).

Acknowledgements

We thank R. Li (Southern University of Science and Technology) for helpful discussion. We are grateful to H. Wang, L. Su and Y. Wu (Institute of Microbiology, Chinese Academy of Sciences), for providing technical assistance in imaging. We are grateful to X. Li and X. Tan for helping with sample preparation and taking SEM images at the Center for Biological Imaging (CBI), Institute of Biophysics, Chinese Academy of Science. We are grateful to T. Zhao (Institute of Microbiology, Chinese Academy of Sciences) for the technical assistance of flow cytometry. This study was supported by the Strategic Priority Research Program of the Chinese Academy of Sciences (grant no. XDB27040210), the Strategic Priority Research Program of Chinese Academy of Sciences (grant no. XDA26030105), the Key Research Program from the Chinese Academy of Sciences (grant no. ZDRW-ZS-2019-2), National Transgenic Major Program (grant no. 2019ZX08010-004), CAS Project for Young Scientists in Basic Research (YSBR-011), the National Science Fund for Distinguished Young Scholars (grant no. 31925003), the National Science

Foundation of China (grant no. 32000142) and the grants from the State Key Laboratory of Plant Genomics.

Author contributions

X.Z. designed and performed experiments, analysed the data, prepared figures and videos, and wrote the manuscript. Q.W. participated in experimental design and technical troubleshooting. J.W. participated in the complementary vector constructions. M.Q. participated in sequence blast and phylogenetic analysis. C.Z., Y.H., G.W., H.W., Y.Y., J.T., D.C. and Y.L. provided essential technical assistances. D.W., Y.Z. and Y.X. participated in data interpretation and manuscript organization. Z.K. conceived the project, interpreted the data, and wrote and revised the article.

Competing interests

The authors declare no competing interests.

Additional information

Supplementary information The online version contains supplementary material available at https://doi.org/10.1038/s41477-022-01261-4.

Correspondence and requests for materials should be addressed to Zhaosheng Kong.

Peer review information *Nature Plants* thanks the anonymous reviewers for their contribution to the peer review of this work

Reprints and permissions information is available at www.nature.com/reprints.

Publisher's note Springer Nature remains neutral with regard to jurisdictional claims in published maps and institutional affiliations.

Springer Nature or its licensor holds exclusive rights to this article under a publishing agreement with the author(s) or other rightsholder(s); author self-archiving of the accepted manuscript version of this article is solely governed by the terms of such publishing agreement and applicable law.

© The Author(s), under exclusive licence to Springer Nature Limited 2022

nature portfolio

Corresponding author(s): Zhaosheng Kong

Last updated by author(s): Aug 12, 2022

Reporting Summary

Nature Portfolio wishes to improve the reproducibility of the work that we publish. This form provides structure for consistency and transparency in reporting. For further information on Nature Portfolio policies, see our Editorial Policies and the Editorial Policy Checklist.

Statistics

For all statistical analyses, confirm that the following items are present in the figure legend, table legend, main text, or Methods section.

n/a	Confirmed
☐	☒ The exact sample size (*n*) for each experimental group/condition, given as a discrete number and unit of measurement
☐	☒ A statement on whether measurements were taken from distinct samples or whether the same sample was measured repeatedly
☐	☒ The statistical test(s) used AND whether they are one- or two-sided *Only common tests should be described solely by name; describe more complex techniques in the Methods section.*
☒	☐ A description of all covariates tested
☒	☐ A description of any assumptions or corrections, such as tests of normality and adjustment for multiple comparisons
☐	☒ A full description of the statistical parameters including central tendency (e.g. means) or other basic estimates (e.g. regression coefficient) AND variation (e.g. standard deviation) or associated estimates of uncertainty (e.g. confidence intervals)
☐	☒ For null hypothesis testing, the test statistic (e.g. *F*, *t*, *r*) with confidence intervals, effect sizes, degrees of freedom and *P* value noted *Give P values as exact values whenever suitable.*
☒	☐ For Bayesian analysis, information on the choice of priors and Markov chain Monte Carlo settings
☒	☐ For hierarchical and complex designs, identification of the appropriate level for tests and full reporting of outcomes
☒	☐ Estimates of effect sizes (e.g. Cohen's *d*, Pearson's *r*), indicating how they were calculated

Our web collection on statistics for biologists contains articles on many of the points above.

Software and code

Policy information about availability of computer code

Data collection	Nikon A1 confocal microscope and PE spinning disk confocal microscope were used to collect microscopic images; ImageJ software was used to collect the data of nodule size and nodule number. Volocity (PerkinElmer, ver 6.2) was used to acquire and assemble image series and 3D reconstruction. DNA content of bacteria was collected by FACSDiva Version 6.1.3 software.
Data analysis	Statistical analysis was conducted using Graphpad prism8; Microscopic images were analyzed by ImageJ software v1.52p. 3D reconstructions of serial slices were conducted with Imaris 9.2.1; Phylogenetic analysis was conducted with MEGA6; Flow cytometry was conducted by FACSDiva Version 6.1.3 software.

For manuscripts utilizing custom algorithms or software that are central to the research but not yet described in published literature, software must be made available to editors and reviewers. We strongly encourage code deposition in a community repository (e.g. GitHub). See the Nature Portfolio guidelines for submitting code & software for further information.

Data

Policy information about availability of data

All manuscripts must include a data availability statement. This statement should provide the following information, where applicable:

- Accession codes, unique identifiers, or web links for publicly available datasets
- A description of any restrictions on data availability
- For clinical datasets or third party data, please ensure that the statement adheres to our policy

The data are available from the corresponding author upon request.

Human research participants

Policy information about studies involving human research participants and Sex and Gender in Research.

Reporting on sex and gender	*Use the terms sex (biological attribute) and gender (shaped by social and cultural circumstances) carefully in order to avoid confusing both terms. Indicate if findings apply to only one sex or gender; describe whether sex and gender were considered in study design whether sex and/or gender was determined based on self-reporting or assigned and methods used. Provide in the source data disaggregated sex and gender data where this information has been collected, and consent has been obtained for sharing of individual-level data; provide overall numbers in this Reporting Summary. Please state if this information has not been collected. Report sex- and gender-based analyses where performed, justify reasons for lack of sex- and gender-based analysis.*
Population characteristics	*Describe the covariate-relevant population characteristics of the human research participants (e.g. age, genotypic information, past and current diagnosis and treatment categories). If you filled out the behavioural & social sciences study design questions and have nothing to add here, write "See above."*
Recruitment	*Describe how participants were recruited. Outline any potential self-selection bias or other biases that may be present and how these are likely to impact results.*
Ethics oversight	*Identify the organization(s) that approved the study protocol.*

Note that full information on the approval of the study protocol must also be provided in the manuscript.

Field-specific reporting

Please select the one below that is the best fit for your research. If you are not sure, read the appropriate sections before making your selection.

☒ Life sciences ☐ Behavioural & social sciences ☐ Ecological, evolutionary & environmental sciences

For a reference copy of the document with all sections, see nature.com/documents/nr-reporting-summary-flat.pdf

Life sciences study design

All studies must disclose on these points even when the disclosure is negative.

Sample size	We chose the sample size and number according to the previous studies in the same field. For ARA assay, we used at least 18 plants each sample. At least 26 plants were used for nodule number and nodule size; Complementary experiment was conducted with 21-79 positive hairy roots; For SEM study, at least 9 nodules were sectioned to take SEM images per sample.
Data exclusions	No data were excluded.
Replication	Every experiment related to statistical analysis and comparison of phenotypes was replicated three times; For qRT-PCR analysis, each experiment was repeated three times independently with similar results; For live-cell imaging, GFP/RFP fluoresce signals were analysed with at least 50 sells from three replications; For SEM studies, at least 9 nodules were sectioned to take SEM images. We considered it was sufficient for SEM analyses particularly if the same structures are seen each time.
Randomization	Sample allocation is not relevant to our study. Comparison of phenotypes was based on different genotypes.
Blinding	Sample allocation is not relevant to our study. Comparison of phenotypes was based on different genotypes. The first author was involved in all experimental data collection.

Reporting for specific materials, systems and methods

We require information from authors about some types of materials, experimental systems and methods used in many studies. Here, indicate whether each material, system or method listed is relevant to your study. If you are not sure if a list item applies to your research, read the appropriate section before selecting a response.

Materials & experimental systems

n/a	Involved in the study
☐	☒ Antibodies
☒	☐ Eukaryotic cell lines
☒	☐ Palaeontology and archaeology
☒	☐ Animals and other organisms
☒	☐ Clinical data
☒	☐ Dual use research of concern

Methods

n/a	Involved in the study
☒	☐ ChIP-seq
☐	☒ Flow cytometry
☒	☐ MRI-based neuroimaging

Antibodies

Antibodies used

The primary antibodies:
anti-α-tubulin from rabbit (Sigma-Aldrich, SAB4500087, polyclonal)
anti-α-tubulin from mouse (Sigma-Aldrich, T5168, B-5-1-2, monoclonal)
anti-GFP from rabbit (Sigma-Aldrich, G1544, polyclonal)
The secondary antibodies:
FITC, Goat Anti-Rabbit IgG(H+L) (EarthOx, E031220)
TRITC, Goat Anti-Mouse IgG(H+L) (EarthOx, E031310)

Validation

All antibodies used here have been validated by manufacturers. The products are intended for research use only and are not to be used for any other purpose, which includes but is not limited to, unauthorized commercial uses, in vitro diagnostic uses, ex vivo or in vivo therapeutic uses or any type of consumption or application to humans or animals.

Flow Cytometry

Plots

Confirm that:

☒ The axis labels state the marker and fluorochrome used (e.g. CD4-FITC).

☒ The axis scales are clearly visible. Include numbers along axes only for bottom left plot of group (a 'group' is an analysis of identical markers).

☒ All plots are contour plots with outliers or pseudocolor plots.

☒ A numerical value for number of cells or percentage (with statistics) is provided.

Methodology

Sample preparation

Nodules of WT and nkcbp mutants were collected and sliced in 0.5 ml of Galbraith buffer containing 1% Triton X-100, nuclei were stained with DAPI (5 μg/mL)

Instrument

flow cytometry (BD FACSCalibur)

Software

FACSDiva Version 6.1.3

Cell population abundance

In the case of bacteria, 30,000 bacteroids were analyzed.

Gating strategy

Firstly, set the FSC/SSC voltage to remove the signals of cell debris and obtain the data P1. Then, adjust the parameter W to obtain the single bacteroid signal P2. Finally, analyze the cells and chose P3 and P4 to make comparisons between WT and mutants (related to Fig. 4g).

☒ Tick this box to confirm that a figure exemplifying the gating strategy is provided in the Supplementary Information.